Shelf/fjord exchange driven by coastal-trapped waves in the Arctic

Mark E. Inall[1,2], Frank Nilsen[3,4], Finlo R. Cottier[1,5], and Ragnhild Daae[3]

[1]SAMS, Scottish Marine Institute, Oban, Scotland, UK, [2]Department of Geosciences, University of Edinburgh, Grant Institute, Edinburgh, UK, [3]The University Centre in Svalbard (UNIS), Longyearbyen, Norway, [4]Institute of Geophysics, Bergen, Norway, [5]Faculty of Biosciences, Fisheries and Economics, UiT The Arctic University of Norway, Tromsø, Norway

Abstract In this article, we show that the class of low frequency (subinertial) waves known as coastal-trapped waves (CTWs) are a significant agent of water volume exchange in a west Svalbard fjord, and by extension more widely along the west Svalbard and east Greenland margins where similar conditions prevail. We show that CTWs generated by weather systems passing across the sloping topography of the shelf break propagate into the fjord, steered by the topography of an across-shelf trough. The CTWs have characteristic periods of ∼2 days, set by the passage time of weather systems. Phase speeds and wavelengths vary seasonally by a factor of two, according to stratification: winter (summer) values are $C_p = 0.25$ ms^{-1} (0.5 ms^{-1}) and $\lambda = 40$ km (84 km). CTW-induced flow velocities in excess of 0.2 ms^{-1} at 100 m water depth are recorded. Observationally scaled CTW model results allow their explicit role in volume exchange to be quantified. Of the estimated exchange terms, estuarine exchange is weakest ($Q_{est} = 0.62 \times 10^3$ m^{3}s^{-1}), followed by barotropic tidal pumping ($Q_{bt} = 2.5 \times 10^3$ m^{3}s^{-1}), with intermediary exchange dominating ($Q_i = 2.4 \times 10^4$ m^{3}s^{-1}). Oscillatory flows display greatest activity in the 1–5 day period band, and CTW activity is identified as the likely source of variability in the 40–60 h period band. Within that band, intermediary exchange driven by CTWs is estimated as $Q_i^{CTW\_ave} = 0.82 \times 10^4$ m^{3}s^{-1}; an exchange rate exceeding both barotropic and estuarine exchange estimates.

1. Introduction

The class of waves known as Coastal-Trapped Waves (CTWs) has long been recognized as an important source of geostrophic variability at subinertial frequencies along the world's ocean margins [*Allen*, 1975; *Huthnance*, 1978; *Mysak*, 1980]. Their explicit role as agents of water property exchange between ocean margins and adjacent coastal systems has received limited attention [e.g., *Proehl and Rattray*, 1984; *Svendsen et al.*, 2002], and for broad fjords (i.e., wide with respect to the Rossby radius) CTWs are an implicit element of what has been termed "intermediary exchange" [see *Stigebrandt*, 2012 and references therein]. However, a detailed examination of CTWs and their effects in fjords is lacking. The purpose of this paper is to analyze velocity records for CTWs in a broad, high-latitude fjordic system, and to quantify their role in water property exchange with the adjacent shelf in comparison to other fjord exchange mechanisms.

The range of potential exchange mechanisms between fjords and their adjacent coastal waters is well reviewed in the literature [*Cottier et al.*, 2010; *Inall and Gillibrand*, 2010; *Stigebrandt*, 2001, 2012]; a brief recap is provided here. Major agents of fjord/shelf exchange are: fresh water input, tides, local winds, and external fluctuations in stratification (usually, remotely wind-forced). Freshwater input at or near the surface drives an estuarine exchange via shear entrainment at the base of the brackish layer. Deep, freshwater input (via sub-glacial discharge) may influence intermediary baroclinic exchange (see below). Tides may drive both barotropic (tidal pumping), [e.g., *Gillibrand*, 2001], and baroclinic exchange (via enhanced diapycnal mixing increasing estuarine exchange). Strong baroclinic tides may also precondition isolated deep water (defined to be those below sill depth), through deep diapycnal mixing, for episodic renewal events [e.g., *Edwards and Edelsten*, 1977]. Local winds may directly drive surface exchange, interacting directly with the estuarine exchange, the balance of the two being expressed via the nondimensional Wedderburn Number [e.g., *Thorpe*, 2005 p. 338]. Local convection can mediate complete fjord basin water renewal, generally on an annual cycle at mid [*Rippeth and Simpson*, 1996] and at high latitudes [*Cottier et al.*, 2005]. In broad fjords (relative to the Rossby deformation radius) a mean, geostrophically balanced lateral circulation can exist.
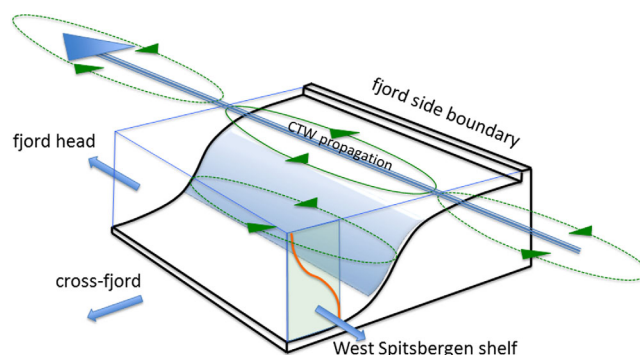
Figure 1. Cartoon schematic of the gravest mode baroclinic CTW: propagating with phase speed C_p along a fjordic boundary in the northern hemisphere. Green ellipses denote horizontal velocities frozen at one moment in time, green arrows indicate direction of flow; solid green is cyclonic flow, dashed is anticyclonic. For clarity, only one lower layer ellipse is illustrated. Note that in reality the ellipse centroids may be virtual; that is, offshore of the domain illustrated rather than above the lower flanks of the slope as shown. The orange curve illustrates a representative vertical density profile. Blue-shaded region is to highlight the slope.

This circulation can be baroclinic, in part a manifestation of the estuarine flow, or barotropic as a topographically steered coastal flow [*Nilsen et al.*, 2015], or a mixture of both [e.g., *Janzen et al.*, 2005; *Svendsen et al.*, 2002]. Finally, changes to the profile of stratification external to the mouth of the fjord can drive what is commonly referred to as intermediary exchange, a term first used by *Stigebrandt* [1990]. Such changes are usually linked to wind-induced coastal convergence or divergence of the surface Ekman layer, leading to coastal downwelling or upwelling, respectively [*Arneborg*, 2004; *Klinck et al.*, 1981]; intermediary exchange has been identified as a major mode of exchange for southeast Greenland's main tide water glacier fjords [*Sutherland et al.*, 2014]. CTWs fall under the category of intermediary exchange, and their general properties are now summarized.

Through a combination of topographic slope, vertical stratification and Earth rotation, subinertial oscillations (CTWs) may be trapped to follow topographic slopes, with their phase propagation direction such that the sloping boundary is to their right (left) in the northern (southern) hemisphere. Generally speaking CTWs take the form of elliptic eddies of alternating sign that propagate along an ocean margin, and may be considered to represent a hybrid between shelf waves (barotropic Rossby waves) and internal Kelvin waves (see Figure 1 for a schematic cartoon, and *Mysak* [1980] for a review of topographically trapped waves). In lakes, baroclinic CTWs have been associated with the generation of cyclonic surface rim currents [*Wunsch*, 1973]. Ocean margins are generally host to topographically steered along-isobath currents, and CTWs not only represent a major source of subinertial variability of these flows [*Allen*, 1975; *Huthnance*, 1978], but may also contribute to their maintenance via wave-induced Stokes Drift [*Weber and Drivdal*, 2012]. At the basin scale, baroclinic CTWs communicate remote pycnocline disturbances, driven by wind or deep convection anomalies, many hundreds or thousands of kilometres on eastern [*Battisti and Hickey*, 1984], and western boundaries [*Johnson and Marshall*, 2002; *Roussenov et al.*, 2008].

Subinertial oscillations in semienclosed coastal systems, such as fjords, have not received a great deal of attention to date. This is in part because many such systems are narrow with respect to the Rossby deformation radius, and the effects of topographic trapping are therefore less evident, though nonetheless may still exist. Additionally, it is observed that superinertial (not subinertial) fluctuations dominate both barotropic and baroclinic variability and exchange in most midlatitude fjordic systems (for reviews of these systems see *Inall and Gillibrand* [2010]; *Stigebrandt* [2012]). However, many wide fjords with weak tides do exist, particularly in the Arctic [*Cottier et al.*, 2010]. This study was partly motivated by very clear evidence of subinertial oscillations in the Strait of Juan de Fuca [*Proehl and Rattray*, 1984], and more strongly motivated by anecdotal evidence that CTWs play an important role in modulating the mean circulation patterns in high-latitude fjords [*Svendsen et al.*, 2002]. In terms of scaling, baroclinic CTWs typically have along slope wavelength of tens to hundreds of km, a period of tens of hours to days, and velocity amplitudes of the order 0.1 ms^{-1}.

For our study of CTWs, we chose the Kongsfjorden system (Figure 2), West Spitsbergen. We refer to the combined fjord and adjacent trough system as Kongsfjorden Trough, shortened to KFT for convenience (noting that the formal Norwegian name for the system is Kongsfjordrenna). The name "Kongsfjorden" and the word "trough" will be retained as necessary to distinguish between fjord and trough. KFT was chosen for a number of reasons: previous studies had hinted at the importance of CTWs in this system [*Svendsen et al.*, 2002]; at high latitude (79°N) the internal Rossby radius is relatively small and the effects of trapping more apparent; previous studies have highlighted the importance of horizontal exchange processes in the
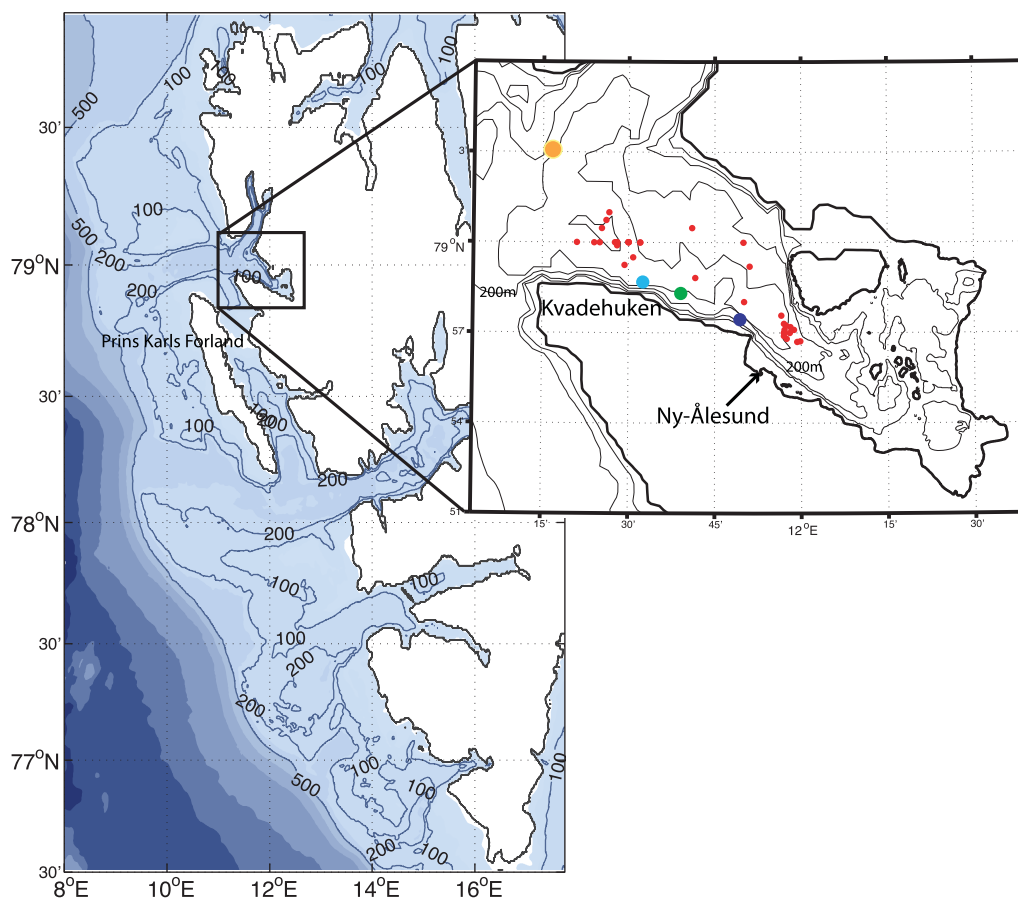
Figure 2. (a) Bathymetry of West Spitsbergen shelf. (b) Map of Kongsfjorden with the two moorings from 2003/2004 to 2004/2005 marked. The cyan and green dots give the position of the UNIS (U1) and the SAMS (S1) moorings during 2003, respectively, the blue dot gives the position of the SAMS (S2) mooring during 2004/2005. The U1 mooring was placed in the same position both years. The red dots are the positions of the historical CTD-stations, the orange dot gives the position of mooring S3.

heat flux divergence of the West Sptisbergen current, the major heat input to the Arctic Ocean [*Boyd and D'Asaro*, 1994; *Cottier et al.*, 2007; *Cottier et al.*, 2005; *Nilsen et al.*, 2008; *Nilsen et al.*, 2006]; and an appropriate data set exists which allows us to determine the properties of CTWs within the KFT system, and to discuss the consequences of the waves on exchange.

The Kongsfjorden-Krossfjorden system opens onto the adjacent West Spitsbergen shelf at a common mouth at 79°N 11′W (Figure 2, and see *Svendsen et al.* [2002] for a multidisciplinary review of the system). Kongsfjorden is the more significant branch of the two-fjord system being both deeper and wider; maximum depths inside Kongsfjorden mouth are ∼350m. A deep, partial sill (maximum depth ∼250m) represents a weak barrier to exchange, exerting negligible exchange control between the fjord system and the trough (see section 5 for justification of this statement), which extends as a deep canyon cutting across the West Spitsbergen shelf. The bathymetry is steep on the southern flank of Kongsfjorden (Figure 2) with a near constant slope of 0.27 between the 50 and 300 m isobaths. This steep boundary is not confined to the fjord and continues westward some 50 km across the shelf and beyond the coastal mouth of the fjord, comprising the southern wall of the trough (Figure 2). West of the fjord mouth the southern boundary of the fjord/trough system becomes comparatively less steep. At approximately half the way along the southern boundary of the trough, at the northern tip of Prins Karls Forland, the typical bathymetric slope has reduced to 0.12. In addition to the more gentle bathymetric slope to the west of the fjord mouth, the coastal boundary becomes detached from the region of steepest bathymetry, giving rise to a shallow shelf to the south of the steep-sided KFT. Such wide shelves are known to alter the properties of CTWs, see for example, *Huthnance* [1978].

Intermediary, balanced geostrophic exchange of water between the fjord and the adjacent shelf is likely "controlled," or at least partially controlled by a geostrophically balanced northward flow, associated with a N/S

aligned frontal system, typically located between the mouth of the fjord and some distance farther west [*Cottier et al.*, 2005; *Nilsen et al.*, 2008]. The concept of "geostrophic control" on intermediary fjordic exchange stems from numerical simulations in a narrow fjord [*Klinck et al.*, 1981]. They showed that following a period of alongshore wind, the perturbation of the lower layer interface is maintained on the coastal boundary in the final geostrophically balanced state (with a geostrophic flow across the mouth of the fjord) restricting further intermediary exchange between fjord and coastal waters even after the alongshore wind relaxes to zero. In that sense, the control of the interface depth at the fjord entrance, which determines the intermediary exchange, is equivalently linked to the steadiness of geostrophic flow across the mouth of the fjord.

Persistence of this geostrophic control requires persistence of the associated N/S aligned frontal system. Perturbations to the frontal position can be forced by anomalous northerly wind bursts (southward wind). Alternatively, complete loss of geostrophic control can occur when a stratification match occurs between fjord and adjacent shelf waters (across the front). Such conditions have been observed during the late summer when solar heating and melt water raise the fjord water vertical stratification to values similar to the adjacent shelf waters [*Cottier et al.*, 2005], under which circumstances the front is no longer maintained at the mouth, and typically northward coastal flow is topographically steered into the fjord.

There has been little investigation of high-frequency variability (periods shorter than a few days) inside Kongsfjord. Barotropic tidal models of the West Spitsbergen/Fram Strait area indicate weak tides, dominated by three semidiurnal constituents (N_2, M_2, S_2) and one diurnal constituent (K_1): with the three semidiurnals of approximately equal amplitude exceeding the diurnal by a factor of two (see also section 2 for tidal velocity analysis inside Kongsfjorden), and an M_2 surface elevation amplitude of approximately 0.5 m at the latitude of Kongsfjorden [*Gjevik and Straume*, 1989; *Padman and Erofeeva*, 2004]. There is a suggestion that regional shelf-wave generation by the K_1 tide may excite baroclinic or barotropic motions within the fjord, characterized by horizontal currents but little surface elevation [*Svendsen et al.*, 2002]. Overall, however, tides are expected to play at most a minor role as an agent of fjord/shelf exchange in the deep-silled fjords of Svalbard and SE Greenland where weak barotropic forcing and a weak baroclinic response prevail; a statement confirmed by recent studies in the two main fjord systems of SE Greenland [*Inall et al.*, 2014; *Sutherland and Straneo*, 2012]. In contrast to the semidiurnal tides, topographically trapped shelf waves with periods of between 24 and 100 h are energetic features of West Spitsbergen shelf flow variability [*Nilsen et al.*, 2006; *Teigen et al.*, 2010]. Low pressure atmospheric systems tracking from west to east over the West Spitsbergen shelf commonly take some tens of hours to pass over a fixed point, and are thought to be an important source of energy for this subinertial variability. All these modes of relatively high-frequency (yet subinertial) variability represent potential forcing mechanisms for barotropic and/or baroclinic mean flow variability within a shelf-adjacent fjord such as Kongsfjord.

The paper is structured as follows: observed stratification and current time series from Kongsfjorden are presented in section 2; a numerical model of CTWs for the observed topography and stratification is introduced in section 3; comparative analysis between model-predicted CTW characteristics and observed CTW structure is presented in section 4; In the discussion of section 5, potential fjord exchange processes are estimated for the KFT system using available data. The wider potential significance to Arctic fjords of CTWs is explored in the second half of section 5; a brief section 6 concludes the paper.

2. Observations

A seasonal climatology of stratification is derived from the historical archive of CTD measurements taken between 1936 and 2007 (Figure 2 and Table 1). Additionally, data from three previously unreported moored current meter deployments are analyzed to describe the variability of flow along the steep southern coastline of Kongsfjorden (Figure 2 and Table 2), and a further current meter record analyzed for baroclinic kinetic energy (Figure 2 and Table 2); the four mooring time series stations are named U1, S1, S2, and S3. Bathymetric data are taken from the IBCAO database [*Jakobsson et al.*, 2012]. Finally, meteorological data from ERA-Interim global atmospheric reanalysis [*Dee et al.*, 2011] are examined as a candidate remote forcing mechanism of CTWs.

Stratification in Kongsfjorden exhibits a strong seasonal pattern [*Cottier et al.*, 2010; *Cottier et al.*, 2005]. Stratification is strongest in summer, and weakest between March and May (Figure 3), as a consequence of

Table 1. Historical CTD Profiles in Kongsfjord

Month(s)	Year
March–May	1965, 2001, 2002, 2002, 2006, 2007, 2007, 2007
June–July	1938, 1958, 2006
August	1936, 1958, 1979, 1981, 1982, 1984, 1985
September	1958, 1968, 1977, 1981, 1982, 1984, 1986, 1990, 1994, 2000, 2001, 2002, 2006
October	1958, 1977, 1978, 1979, 2007
December	1994

strong heat loss to the atmosphere, but rarely resulting in ice cover at any of the four mooring locations (see Figure 2). During the winter/spring (lowest stratification), period from March to May stratification is near uniform in the vertical with typical Brunt-Väisälä frequency values of $N = 1.8 \times 10^{-3}$ s^{-1}. In contrast, stratification is strongest in summer between August and September, with a near surface peak in N of around 2×10^{-2} s^{-1} and an approximately exponential decay with depth to values of $N = 2 \times 10^{-3}$ s^{-1} at a depth of 300 m (Figure 3). Glacial melting and solar heating both contribute to this seasonal peak in fjord stratification.

Unfiltered velocity time series from U1 (Figures 4a and 4b) show peak velocities over a three and a half month period of $+0.29$ ms^{-1} and $+0.07$ ms^{-1} in across and along-isobath components, respectively (positive flow into the fjord and towards shallowing isobaths). Along-isobath velocities have greater temporal coherence (more energy at low frequency) than do the across-isobath velocities, a result of the proximity of the moorings to the shore, although there appears to be a high level of coherence between along and across-isobath components during a number of low-frequency "event" periods. The mean along-isobath flow at U1 is $+0.04$ ms^{-1} and $+0.02$ ms^{-1} at 94 and 44 m, respectively (positive flow into the fjord), with greater variance in the shallower time series; σ (std dev.) $= 0.05$ ms^{-1} and $\sigma = 0.08$ ms^{-1} at 94 and 44 m, respectively. These mean values are broadly consistent with the lateral circulation reported by *Svendsen et al.*, [2002].

The geographic and oceanographic context of KFT can be translated into typical values of the Burger number, $S = (NH/fL)^2$ (the relevant nondimensional parameter for low frequency (subinertial) waves in stratified flow over sloping boundary); H/L is the topographic slope, N the buoyancy frequency, and f the Coriolis parameter. For values of these parameters representing the seasonal and spatial variations relevant here, the Burger number at the mouth of Kongsfjorden ranges from $S \sim 20$ in March (winter) to $S \sim 800$ in September (summer). Farther west, and on the southern flanks of the trough at the longitude of the northern tip of Prins Karls Forland (Figure 2), the Burger number has a seasonal minimum value of $S \sim 3$. Persistently high values of S (i.e., $S > 1$) in the fjord indicate an expected dominance of stratification in the vertical over the effects of Earth rotation and potential vorticity conservation on the behavior of the time varying flow. In the context of CTWs, this leads to the expectation that any observed waves will be only weakly effected by rotation (horizontally nondivergent) and predominantly rectilinear along the coast. In wave terminology, we expect weakly rotationally modified baroclinic Kelvin waves to exist along the southern boundary of the fjord and adjacent trough, with

Table 2. Moored Current Meters, Temperature, and Salinity Loggers: Positions, Durations, and Instrument Types[a]

Instrument	Parameters	Depth (m)	Start	Stop	Sample
Station U1 (UNIS): Position 78 58.681N, 11 32.490E. Water Depth = 202 m					
RCM9MkII	TCDVP	44	28 Sept 2002	6 Sept 2003	1 h
RCM9MkII	TCDVP	94	28 Sept 2002	6 Sept 2003	1 h
RCM9MkII	TCDVP	184	28 Sept 2002	6 Sept 2003	1 h
RCM9MkII	TCDVP	44	23 Aug 2004	11 Sept 2005	1 h
RCM9MkII	TCDVP	94	23 Aug 2004	24 Jan 2005	1 h
RCM9MkII	TCDVP	184	23 Aug 2004	19 July 2005	1 h
Station S1 (SAMS 1): Position 78 58.307N, 11 39.114E. Water Depth = 260 m					
RDI ADCP 300 kHz	UVW	120–50 m in 4 m bins	23 May 2003	6 Sept 2003	20 min
Station S2 (SAMS 2): Position 78 57.443N, 11 49.365E. Water Depth = 170 m					
Minilog	T	71	22 Aug 2004	14 Sept 2005	1 h
Minilog	T	111	22Aug 2004	14 Sept 2005	1 h
Minilog	T	157	22 Aug 2004	14 Sept 2005	1 h
RDI ADCP 300 kHz	UVW	132–20 m in 4 m bins	23 Aug 2004	14 Sept 2005	20 min
Station S3 (SAMS 3): Position 79 03.25 N, 11 18.00E. Water Depth = 215 m					
RDI ADCP 300 kHz	UVW	145–29 m in 4 m bins	16 Apr 2002	28 Sept 2002	20 min

[a]ADCP was an RD Instruments 300 kHz Sentinel ADCP; RCMs were Aanderaa Instruments RCM9MkII with integral CTD sensors. Minilogger were 12 bit Vemco temperature loggers.
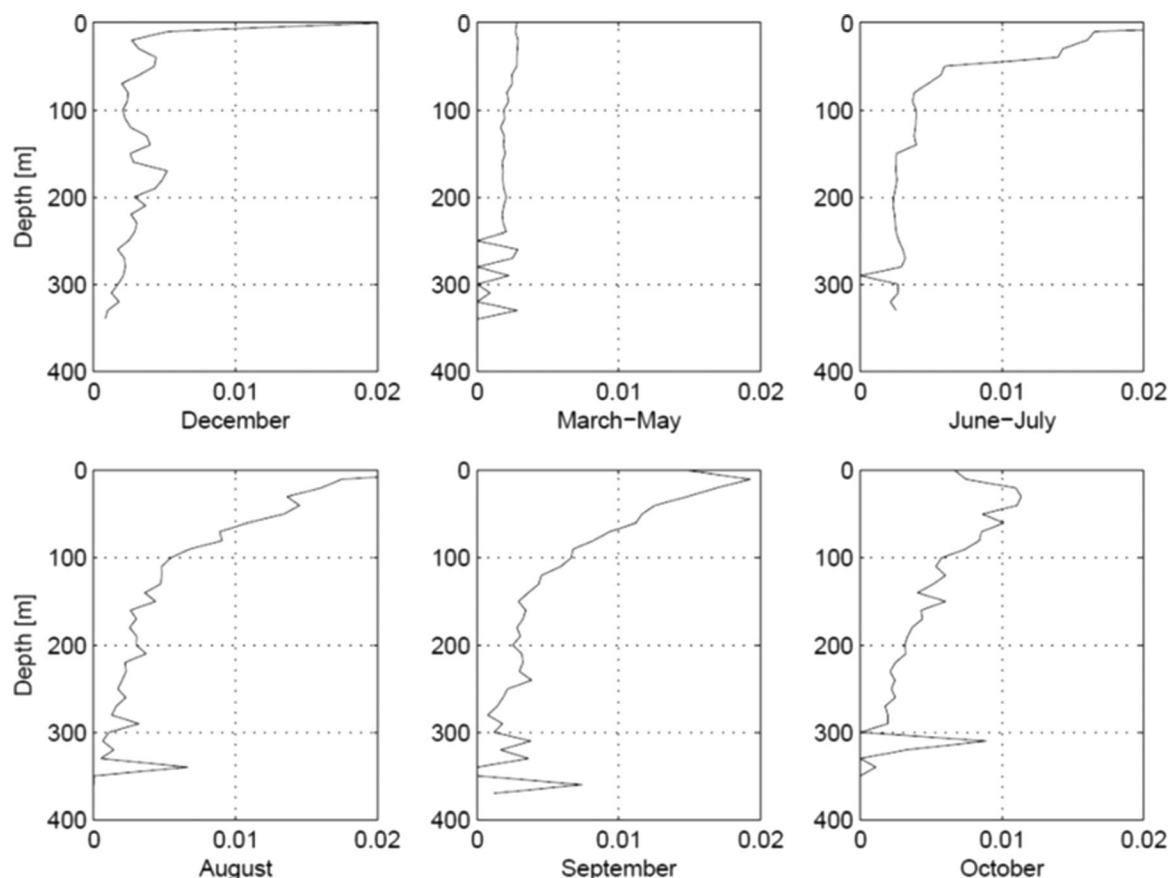
Figure 3. Seasonal variations in stratification (N, s^{-1}): derived from the historic CTD database of Table 1, with the range of positions indicated in Figure 2, and time averaged is as indicated in each plot. Number of CTD profiles used in each averaging interval: December = 18, March–May = 197, June–July = 1570, August = 998, September = 595, and October = 34.

the rotational component diminishing as the bathymetric slope increases eastward along the southern boundary of KFT from the ocean margin and into the fjord proper.

With $S \geq 1$ CTWs will be predominantly rectilinear; nevertheless, rotary spectra [*Gonella*, 1972] are used because we do not assume a priori that Kelvin waves are present, and, having established their presence, rotary spectra help determine the position of the moored current meters with respect to the center of the current ellipses. Rotary spectra at the 94 m level for the U1 mooring time series from May 2003 to September 2003, and for the S2 mooring time series from October 2004 to January 2005 are shown in Figures 5a and 5b, respectively. The semidiurnal and diurnal tidal bands clearly stand out as phase coherent signals in the spectra, although harmonic tidal analysis reveals that very little (1.2%) of the total variance in the velocity time series is of tidal origin (Table 3).

A broader and less distinct local energy maximum is seen at longer periods, between 30 and 60 h, in both mooring time series analyzed (U1 and S2). This range of periods is examined in more detail and it is shown that the wider energy maximum is due to the intermittent occurrence of CTWs along the sloping flank of KFT. The rotary spectra (Figures 5a and 5b) reveal that the anticyclonic rotating component contains marginally more energy than the cyclonic component (although the statistical significance of the difference at any given period is weak). With the coastline to the right, this small difference is consistent with vorticity wave center (i.e., the across-isobath position of the CTW ellipse center, see cartoon of Figure 1) being situated to the left (looking into the fjord in the direction of wave propagation) of our current meter time series, i.e., the ellipse center is downslope from our mooring positions. Thus, the rotary spectra are consistent with the passage of a vorticity-modified Kelvin wave in the period band of 30–60 h, in itself consistent with the large Burger number ($S > 1$).

Wavelet analysis is used to look at the time variation of the amplitude of harmonic variability in the (scalar) current speed time series. Since the predicted waves are Kelvin-like, with a relatively small across-isobath
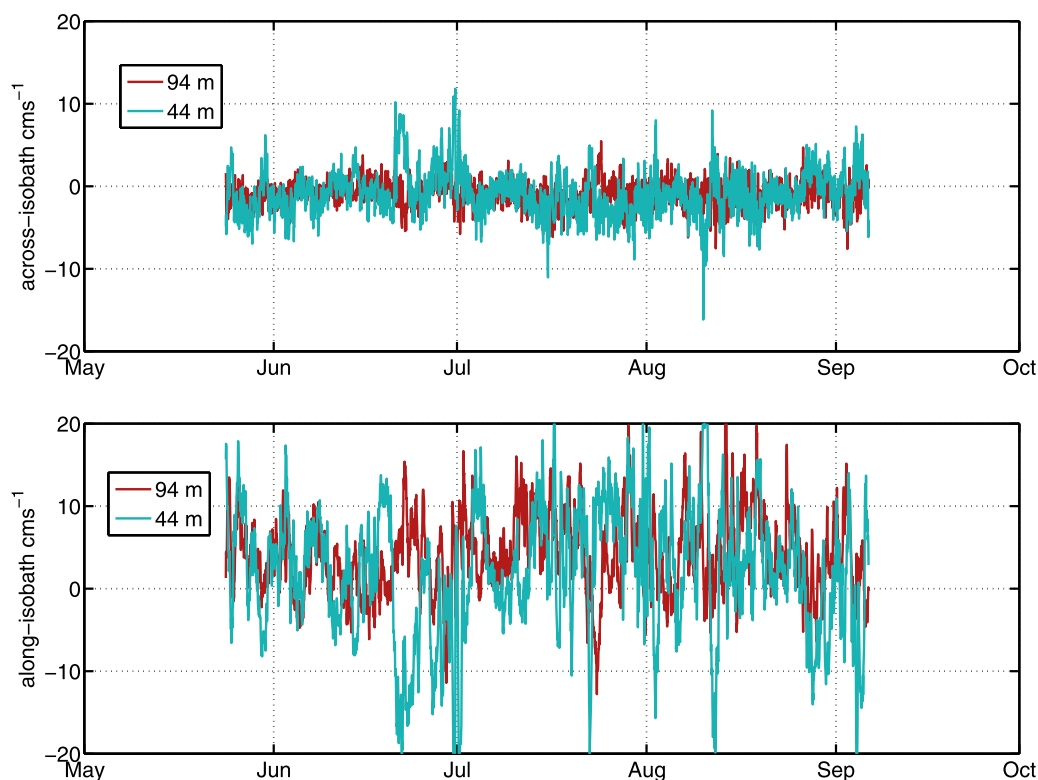
Figure 4. (top) Across-isobath and (bottom) along-isobath velocity time series recorded at 94 m and 44 m at the U1 mooring, May–September 2003.

flow, wavelet analysis is performed only on the along-isobath component of velocity. Analyses of summer and winter along-isobath velocities from the U1 mooring at 94 m are presented in Figures 6a and 6b. In neither spectrum (summer nor winter) are the semidiurnal species significant at the 95% confidence level. There are periods during summer when the diurnal variation is significant, but the most obvious band of significant harmonic variability occurs in episodic events in a band of periods ranging between 30 and 60 h. A particularly strong (and broader bandwidth) event in November 2004 (Figure 6b) is most likely in response to a severe winter storm, a point we return to later. In the summer, four of five "events" occur between late June and early September during which time significant along-isobath current variability is apparent with a periods of several tens of hours.

At this stage in the analysis, we have introduced the expectation, based on a discussion of the literature, that there is a strong likelihood of finding significant CTW activity in the troughs and fjords west of Svalbard. Further, through time series analysis on individual records we have identified signals in the velocity spectra at the fjord entrance that indicate substantial subinertial oscillating flows with periods in the 30 to 60 h period band, suggestive of the presence of CTWs. The evidence presented so far, however, is by no means conclusive. We now go on to investigate, with the use of a CTW wave model, what the predicted spatiotemporal structure of CTWs with a period of many tens of hours in this particular system (geometry and stratification) should look like. We then seek evidence of this predicted wave structure in the observed time series by performing more in-depth time series analysis which makes use of quantified coherence and phase information between adjacent moored time series.

3. Trapped Wave Model

Following *Brink* [1982], we calculate the free wave solutions for linearized coastal-trapped waves along a straight and uniform coastline. The offshore direction is *x*, the alongshore direction *y*, and the vertical direction *z*. Stratification is represented by a surface intensified buoyancy frequency profile, decreasing exponentially with a vertical scale z_0; represented by $N^2(z) = N_0^2 exp(z/z_0)$. Two extremes of stratification
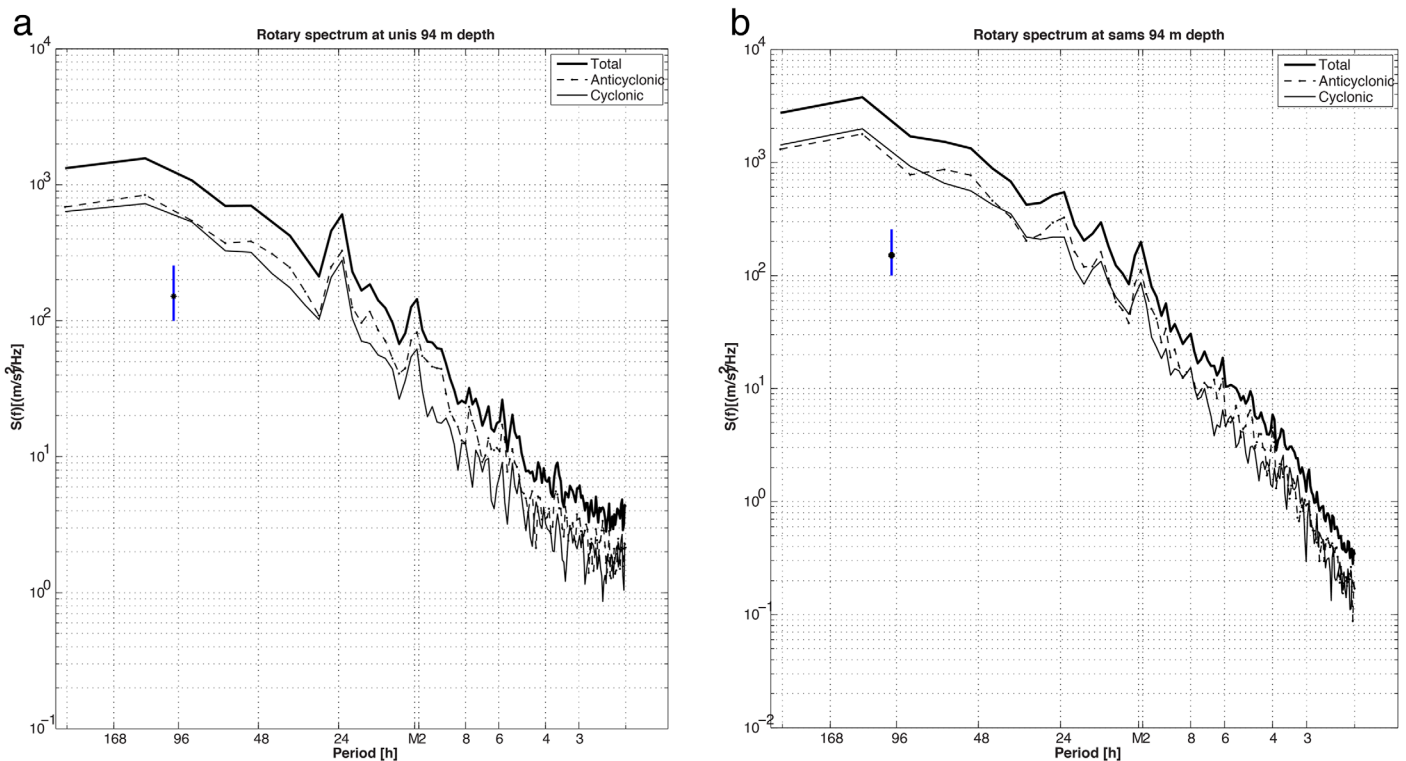
Figure 5. Rotary spectral analysis of U1 and S1 mooring velocity time series at 94 m. Total, cyclonic, and anticyclonic in bold, continuous, and dashed black lines. 95% confidence limits in blue. (a) U1, May–September 2003. (b) S1, 11 October 2004 to 24 January 2005.

are investigated in the numerical simulations, representing winter conditions (March) with low stratification, $N_0^2 = 1 \times 10^{-5} \text{ s}^{-2}$ and $z_0 = 300$ m, and summer conditions (August/September) with higher stratification, $N_0^2 = 3.8 \times 10^{-4} \text{ s}^{-2}$, and greater surface intensification, $z_0 = 50$ m. The sloping topography is represented using a functional form following *Dale et al* [2001] equation (49).

$$h(x) = \begin{cases} h_c + (h_{match} - h_c)x/x_{match}, & x \leq x_{match} \\ h_s + \frac{1}{2}\left\{1 - \cos\left[\frac{\pi}{W}(x - x_s)\right]\right\}^{3/4}(h_0 - h_c), & x_s + W > x > x_{match} \\ h_0, & x \geq x_s + W \end{cases} \quad (1)$$

where, h_c, h_s, and h_0 are the water depths at the coastal wall ($x = 0$), at the shelf edge, and at the base of the slope, respectively; W is the width of the sloping region. The shelf slants linearly to a depth of h_{match} at $x = x_{match}$ with values chosen such that the depth and gradient of the shelf and slope match, and in practice are very close to h_s and x_s. Two examples of topography are chosen to represent the range of along slope variations on the southern flank of the KFT system: Case 1), the steeper Kongsfjorden coast between Kvadehuken and Ny-Ålesund where the moorings were located (Figure 2), with a narrow shelf (hereafter termed "KF") with slope parameter values: $h_c = 5$ m, $h_s = 20$ m, $h_0 = 300$ m, $W = 1200$ m, and $x_s = 100$ m; and Case

Table 3. Tidal Analysis of Barotropic (Depth-Averaged) Currents at S2 (ADCP Mooring)[a]

Constituent	Freq.	Major (ms^{-1})	Minor (ms^{-1})	Inclination CW from N	Phase	snr
K_1	0.04178	0.00189	−0.00042	161.3	159.0	1.3
N_2	0.07900	0.00120	0.00020	141.6	36.8	4.3
M_2	0.08051	0.00805	−0.00006	149.4	90.3	180
S_2	0.08333	0.00265	−0.00007	152.9	132.2	19

[a]Taken together these four constituents capture only 1.2% of the velocity time series variance. All other resolvable tidal constituents have a signal to noise ratio (snr) of less than one.
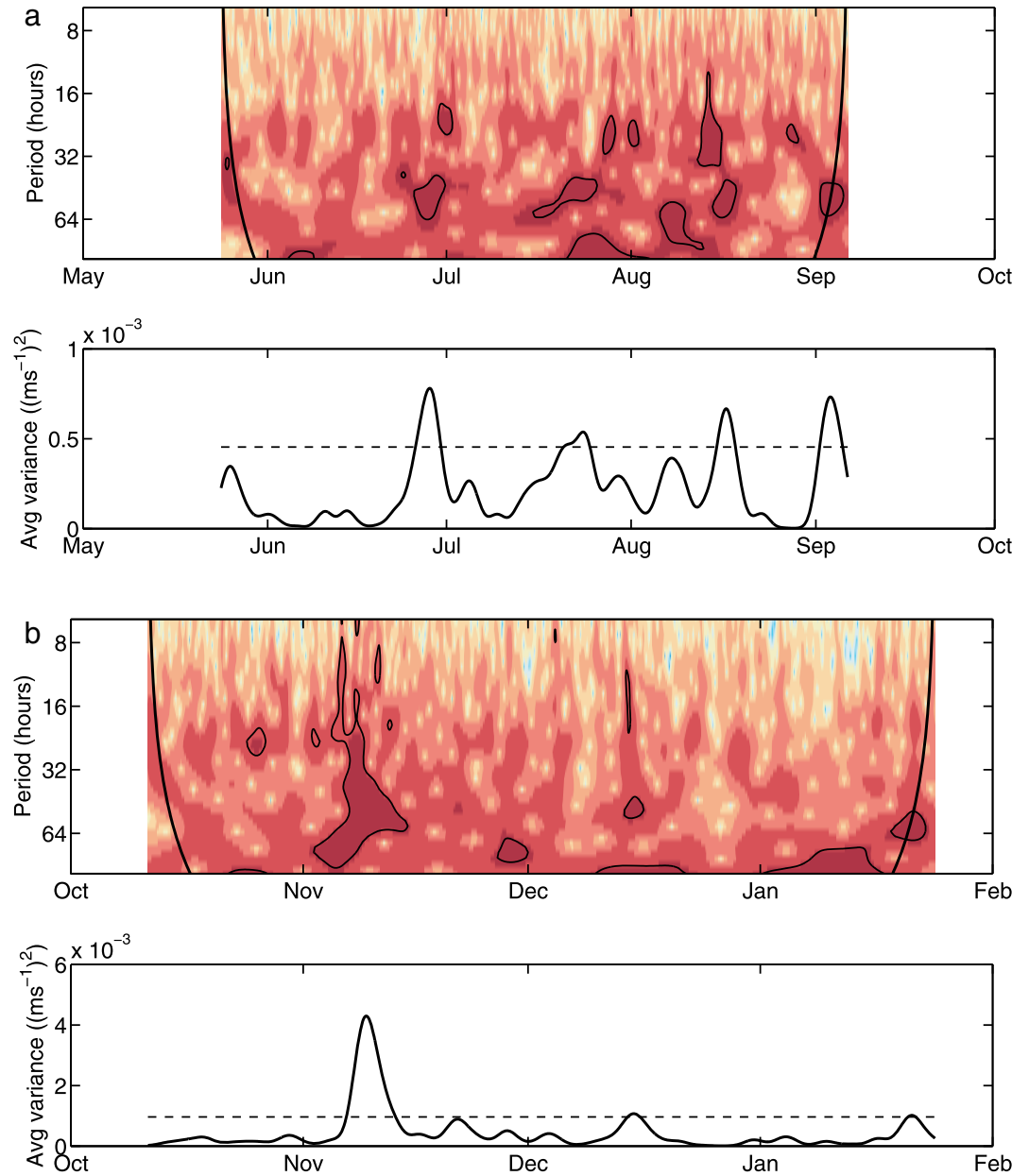
Figure 6. Wavelet analysis of along-isobath deep velocity (94 m) from the U1 mooring. (a) May–September 2003. (b) 11 October 2014 to 24 January 2005. (top) Black contours indicate significance at the 95% confidence level. (bottom) Scale-averaged variance over the 40–60 h period band (solid curve), 95% significance level indicated with a gray-dashed line.

2), the less steep southern flank of the trough north and due west of the tip of Prins Karls Forland, where the shelf is considerably wider (hereafter "PKF") with slope parameter values: $h_c = 40$ m, $h_s = 40$ m, $h_0 = 250$ m, $W = 2000$ m, and $x_s = 5000$ m. These analytic forms closely follow the observed topography to an extent to which it is known. The upper slopes and shallows are least well mapped, which is why we chose to represent the topography analytically as described. For both cases 1 and 2, the model domain was 300 m deep, and 3 km wide for case 1 (KF, narrow shelf), and 9 km wide for case 2 (PKF, 5 km wide shallow shelf), with 200 horizontal grid points ($\Delta x = 15$ m for case 1 and $\Delta x = 45$ m for case 2) and 30 grid points in the vertical ($\Delta z = 10$ m). Four model simulations are considered in detail: termed KF_w (case 1 Kongsfjord winter), KF_s (case 1 KF summer), PKF_w (case 2 Prins Karls Forland winter), and PKF_s (case 2 PKF summer). Model sensitivity was also investigated with respect to open or closed offshore boundary conditions and with respect to an imposed alongshore mean current. Imposing an along-isobath current does decrease
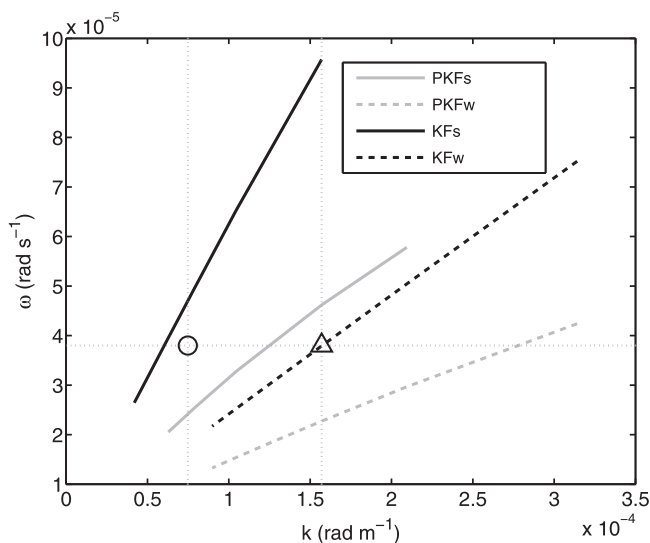
Figure 7. Modeled dispersion relation for summer (s) and winter (w) stratification at two locations along the KFT axis: one representative of the moorings position (KF) and the other at the northern tip of Prinz Karls Forland (PKF). The two vertical lines are located at wavelengths of 84 km (left) and 40 km (right), and the horizontal line is drawn at a period of 46 h. Placed on the $T = 46$ h line are two symbols representing the observed wave properties in summer (circular symbol) and winter (triangular symbol).

wave frequency for a given wavenumber, with greater effect when stratification is weaker. The effect of a maximum along-isobath flow of 0.04 ms^{-1} (equal to the mean observed along-isobath current at 94 m) was investigated for winter and summer conditions at both locations (KF and PKF). The across-isobath mean flow structure was set to mimic the mean current structure seen by *Svendsen et al.* [2002], with a maximum flow over the midslope and horizontal exponential decay scales of 2 km (offshore) and 500 m (onshore), and a vertical exponential decay scale of 100 m above and below the core. Model sensitivity to the choice open or closed offshore boundary was found to be negligible. The effect of the mean flow on the dispersion curves was relatively small, decreasing the frequency by less than 2% of its value for summer stratification, and up to 15% for winter stratification. In all four reported simulations, the offshore boundary was left open, and the coastal boundary closed, appropriate for the geometry of the system under investigation, but noting the model insensitivity to this choice.

Given the anticipated CTW activity with a period of several tens of hours, four dispersion curves were computed for frequencies covering the range $\omega = 1 \times 10^{-5}$ to 1×10^{-4} s^{-1} (wave periods of between approximately 174 and 17 h), and for along-isobath wave numbers between $k = 0.4 \times 10^{-4}$ and 3.4×10^{-4} m^{-1} (corresponding to along-isobath wavelengths between 157 and 18 km). Dispersion curves for conditions of zero along-isobath flow are presented in Figure 7 (as noted, the mean flow of 0.04 ms^{-1} has only a modest effect on the curves). The first point to note is that all the dispersion curves to a first approximation are straight lines, that is the phase speeds are constant, consistent with the notion that these are long, nondispersive waves, with their propagation speed determined by the stratification and topography. The second point to note is that waves with period of 40 h ($\omega = 4.36 \times 10^{-5}$ s^{-1}), a value somewhere in the midrange of the band of significant harmonic variability revealed by the rotary and wavelet analysis, have
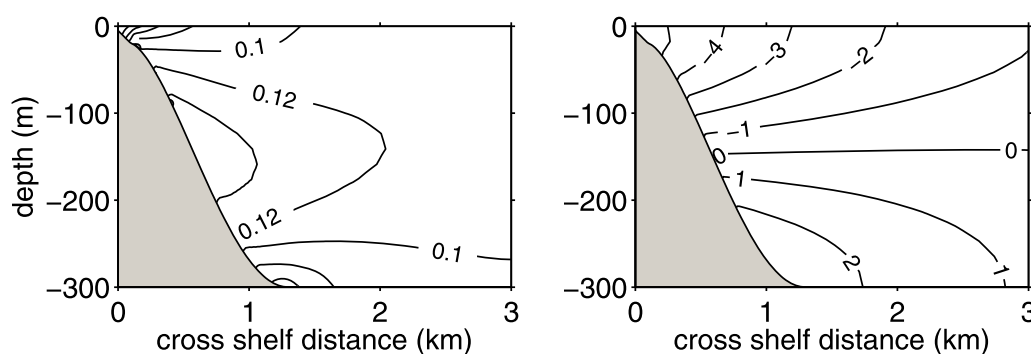

Figure 8. Modeled velocity field structure for winter at the mouth of fjord near mooring locations: (left) across-isobath and (right) along-slope. Scaling is arbitrary. The corresponding location on the dispersion curve is indicated by a triangle in Figure 7.
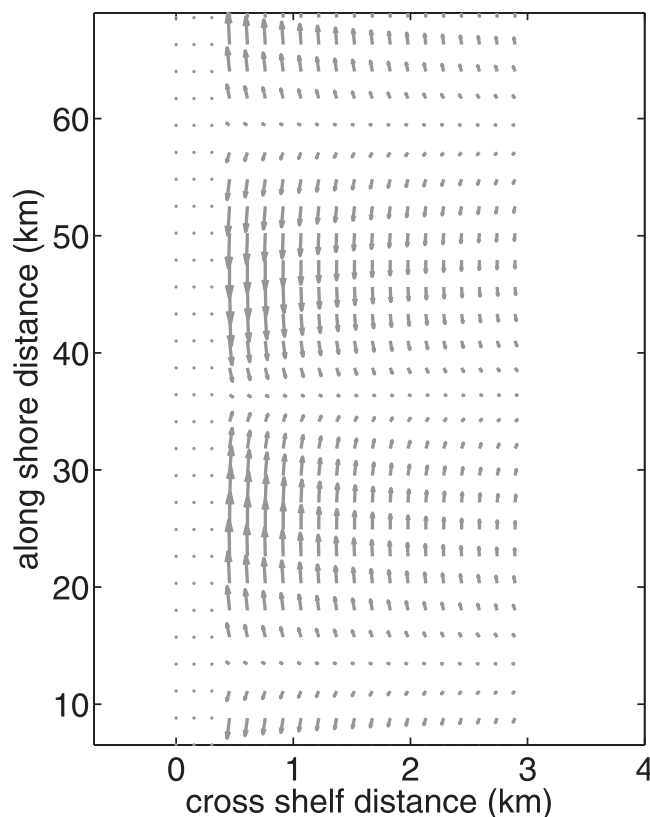
Figure 9. Reconstructed unscaled modeled velocity field at a depth of 100 m for the same model configuration as Figures 7 and 8.

wavelengths ranging from 22 km ($k=2.86\times10^{-4}$ m^{-1}, experiment PKF_w) to 114 km ($k=5.51\times10^{-5}$ m^{-1}, experiment KF_s).

Taking the specific case of winter stratification at the fjord mouth (experiment KF_w), and selecting a wave period of 46 h (the reader is referred forward to the phase coherence analysis of section 4 for an explanation of this precise choice), the model predicts trapped waves with an along-isobath wavelength of 40 km; this point on the dispersion curve is indicated with a triangle symbol.

Modeled waves at this point on the KF_w dispersion curve have a mode one structure in the vertical; illustrated, for example, in the across-isobath velocity field structure (Figure 8, scaling is arbitrary). Flow is surface intensified, with a zero crossing of the along-isobath velocity at around 150 m, and a low mode across-isobath structure with along-isobath surface velocities decreasing by a factor of 5 at a distance of around 3 km from the coastal boundary, and near-bed along-isobath velocities decreasing less sharply (a factor of 2.5 over a similar distance). Across-isobath velocities (and vertical velocities, not shown) peak at the region of the steepest slope at around 150 m, and are typically two orders of magnitude smaller than along-isobath velocities. This same basic wave structure is found for all wave solutions of the dispersion curves shown in Figure 7; that is, all dispersion curves shown represent the lowest vertical mode.

From the solutions for the wave structure at one particular point in $k\omega$-space (as shown in Figure 7), it is possible reconstruct a spatial representation of the modeled horizontal velocity field at a depth of 100 m for the same model configuration as Figure 8. This is shown in Figure 9, and gives a clear visual representation of an instantaneous planar view of the wave field at this depth, which is consistent with the cartoon schematic of Figure 1. This viewpoint clearly shows the near-rectilinear nature of the wave, the offshore decay, and the presence of a (virtual) ellipse center beyond the (open) offshore model boundary (and beyond the moorings in real space). Another viewpoint for the modeled waves is to reconstruct a horizontal time series at an equivalent location to one of the moored current meters. This view is shown in Figure 10 for a depth of 100 m at a location representative of the S2 mooring location. For later comparison, the observed equivalent signal is also shown in Figure 10.

4. Comparative Analysis: Model and Observations

Complex coherence methods reveal how a rotating current vector measured at one position corresponds to the rotations of a current vector measured at another position in space. The inner coherence spectrum (the modulus of the complex inner coherence) gives the corotating response, whereas the outer coherence spectrum gives the counter rotating response. The current vectors rotate in an anticyclonic sense on the left hand side and in a cyclonic sense on the right hand side of the inner coherence spectra. The phase spectra (the argument of the complex coherence estimate) can be used to calculate the wavelength λ of a signal with known frequency ω. Assuming a plane wave solution, and that the wave signal passing a
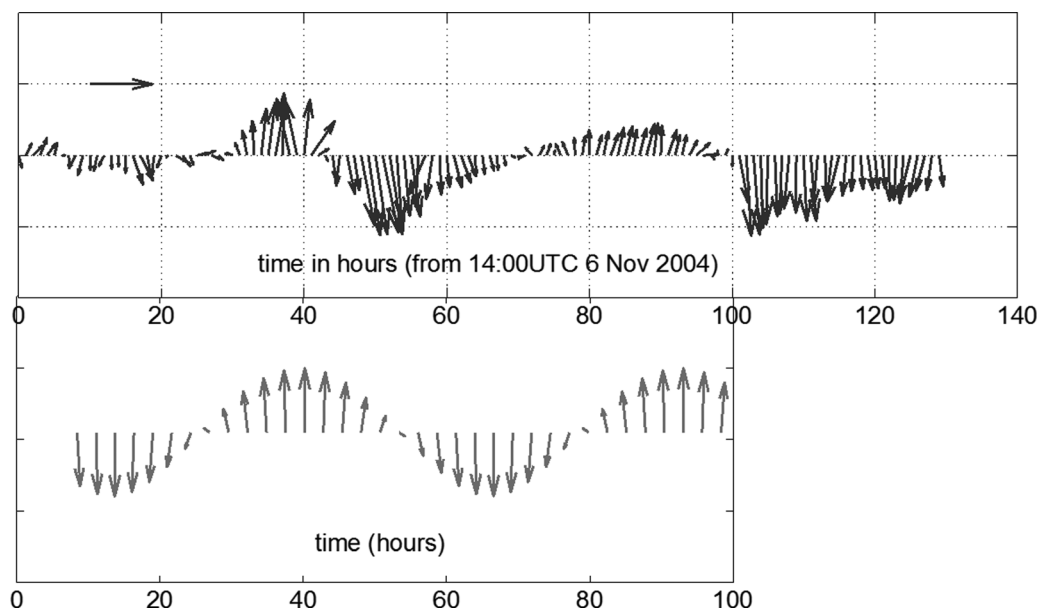
Figure 10. Observations of the velocity field at 94 m during the period 5–11 November 2004 from the S2 mooring. Vectors have been rotated such that vertical, upward pointing vectors correspond to along slope currents directed into the fjord. Scale arrow is 0.25 ms^{-1}; (top) the maximum observed vector has length corresponding to 0.32 ms^{-1}. Reconstructed unscaled modeled velocity time series at a depth of 100 m for the location of the S2 mooring, again using the same model configuration as Figures 7–9.

mooring A at time t_0 is delayed by a phase difference $\Delta\phi$ when passing a mooring B, the wavelength λ for a particular significant frequency signal can then be found according to

$$|\lambda| = \left| \frac{2\pi}{\Delta\phi} L \right|, \tag{2}$$

where $\Delta\phi$ is the phase difference in radians and L is the distance between the two moorings [*Nilsen et al.*, 2006]. Furthermore, the phase speed, C_p, for a given period, T, can then be calculated simply as $C_p = \lambda/T$.

Several episodes of significant harmonic variability with periods in the 30–60 h waveband have already been identified in the wavelet analysis of individual moored time series presented in section 2 (Figures 6a and 6b). Furthermore, the CTW model simulations appropriate for all three mooring locations on the southern edge of Kongsfjorden (U1, S1, and S2, Figure 2) predict quite different dispersion curves for stratification profiles typical of winter and summer (Figure 7). Thus, two separate sets of coherence and phase spectra are computed; one pair corresponding to winter (Figure 11), the other to summer (Figure 12).

The anticyclonic side of the inner coherence spectrum in Figure 11 (winter case) shows that there is a peak at a period of approximately $T = 46$ h within the broad 35–48 h period bandwidth, with a coherence of 0.88. The corresponding phase lag is approximately 1 radian, and the wavelength is calculated to be $\lambda = 40$ km. Using $T = 46$ h, the phase speed may be estimated, giving $C_p = 0.24$ ms^{-1}. Hence, this analysis of the current meter data at 94 m shows significant anticyclonic corotating velocity vectors at both the U1 and S2 moorings that can be explained by a 40 km long vorticity wave with a vorticity center farther off-coast relative to the current meter moorings, and propagating along the coast with a phase speed of $C_p = 0.24$ ms^{-1}.

As shown by the dispersion curves derived using the CTW model (Figure 7), the waves are nondispersive around the 40 h period band, i.e., the phase and group velocities are equal. The group velocity can be independently calculated from coherence estimates (Figure 11) if the phase decrease or increase is linear with frequency [*Livingstone and Royer*, 1980]. First, the time lag $\tau = t_B - t_A$ between two moorings can be found by assuming that a signal that passes mooring A at t_A, reaches the next mooring B at t_B. The phase difference between the two moorings is then given by
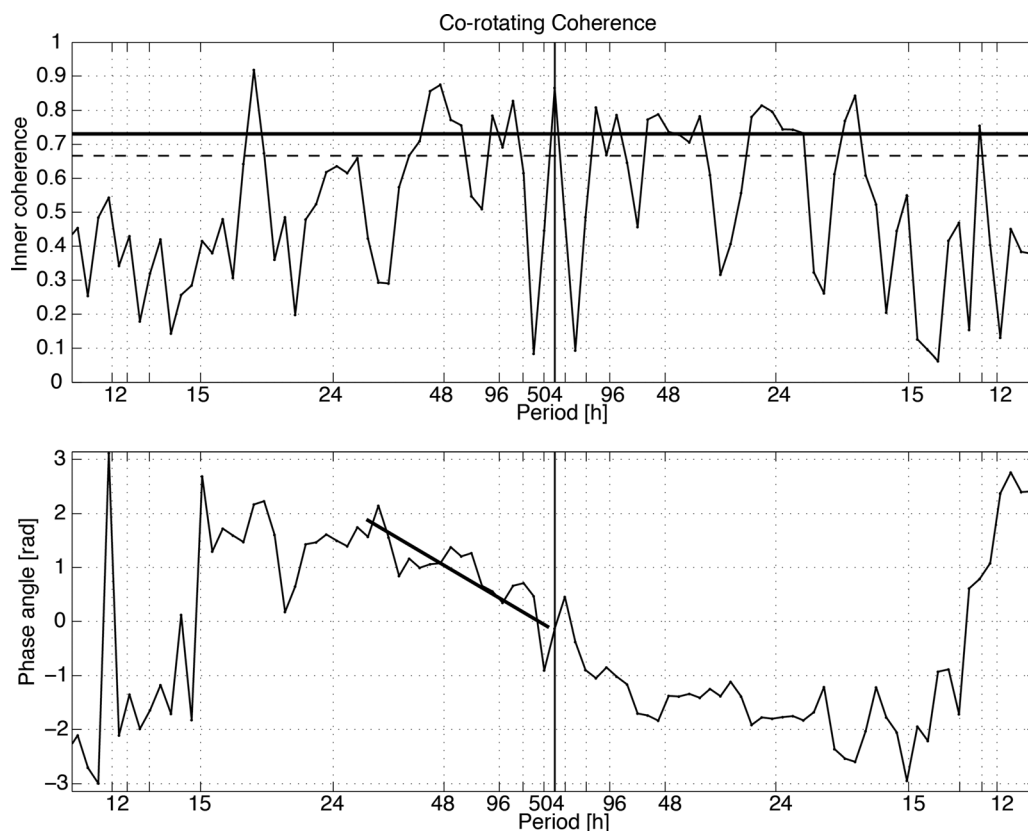
Figure 11. (a, top) Inner coherence and, (b, bottom) phase spectra between the U1 and S2 moorings at 94 m depth between 11 October 2004 and 24 January 2005 with the 90% (dashed) and 95% (solid) confidence level. The strait line in the phase spectrum shows the slope used to calculate the time lag between the two moorings.

$$\phi_{AB}(\sigma) = 2\pi\sigma(t_B - t_A) = 2\pi\sigma\tau, \tag{3}$$

where $\sigma = 1/T$. If the time-lag τ is constant with respect to frequency σ, the phase spectrum should be a linear function of the frequency with a constant gradient $d\phi/d\sigma$, and the time lag can be expressed as,

$$\tau = \frac{1}{2\pi}\frac{d\phi}{d\sigma} \tag{4}$$

In Figure 11b linear decrease of phase with frequency is identified in the 35–48 h waveband of interest, and we find that in this region $\tau \approx 7$ h. The mean advection speed or the wave group velocity along a line between mooring stations is then given by $C_g = L/\tau \approx 0.25$ ms^{-1}. Hence, the current meter data confirm that phase and group velocities are equal for vorticity waves around the 40 h period band, consistent with the findings of the model.

For stratification typical of summer, a similar analysis is performed. Figure 12 illustrates a summer example when the current meter moorings had concurrent measurements from 24 May to 6 September 2003. There is more energy on the cyclonic rotary side compared to the winter case (Figure 12), but an anticyclonic coherence maximum in the 35–48 h period band is also pronounced in the summer data when the stratification is stronger. The highest peak (0.89) on the anticyclonic rotary side is again found at approximately 46 h with a phase lag of 0.48 radians. The estimated summer wavelength and phase speed are therefore $\lambda = 84$ km and $c = 0.5$ ms^{-1}, respectively. Hence, the wavelength and phase speed have doubled compared to the winter case study, which can be explained by a stronger vertical stratification and is consistent with the modeled dispersion curves.

We now return to the modeled dispersion relation (Figure 7) and plot on this diagram the winter and summer CTW properties derived from the coherence and phase analysis presented above. Acceptable agreement is found for summer (Figure 7, open circle) and near-perfect agreement for winter (Figure 7,
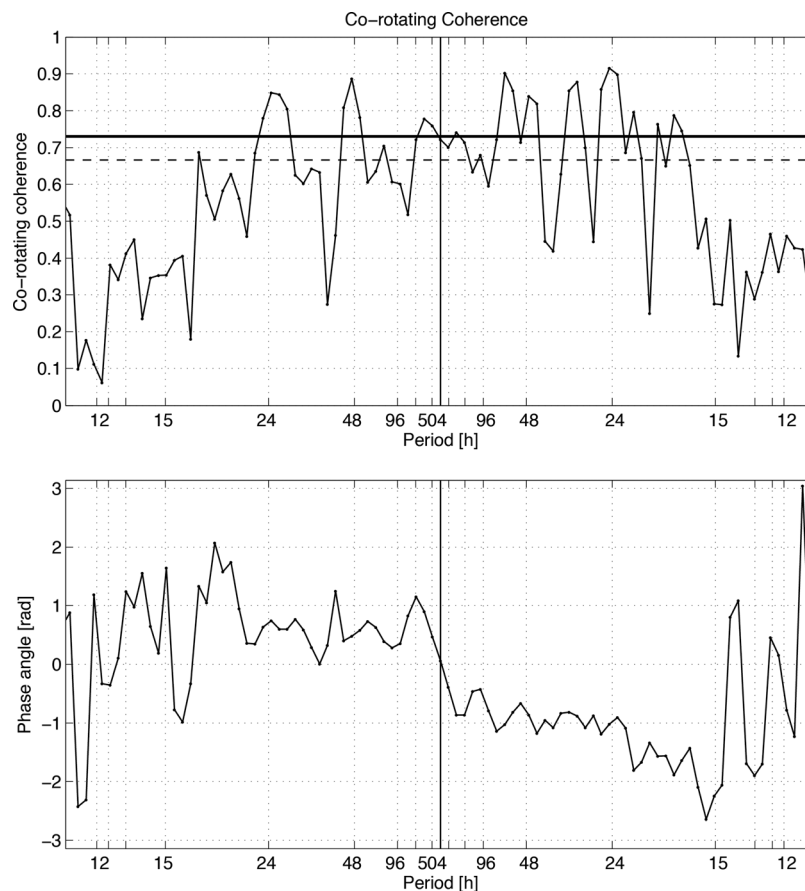
Figure 12. (a, top) Inner coherence and, (b, bottom) phase spectra between the U1 and S2 moorings at 94 m depth between 24 May and 6 September 2003 with the 90% (dashed) and 95% (solid) confidence level.

open triangle). We may speculate why winter is a near-perfect match and summer is just acceptable. Winter is generally a situation with weak stratification and rather little variation through the season. In summer, the mean profile of stratification probably has more significant variability associated with it, and so it is less likely that the mean profile used will be an accurate representation of reality during the time of mooring deployment.

4.1. Scaling of Modeled CTWs

To enable discussion of the potential effects of CTWs on fjord exchange, the reconstructed modeled velocity fields are scaled by the observed wave-induced velocities. Taking the observed CTW signal in Figure 10, a maximum velocity amplitude of 0.32 ms^{-1} is observed at 94 m depth. This is one of the strongest of the observed CTW signals (and indeed a peak speed faster than the winter average phase speed). Taking a harmonic fit to these observations yields a CTW velocity amplitude estimate of 0.20 ms^{-1}; a more appropriate value to use for model scaling. We may then scale the modeled along slope velocity field by this value, noting that the observation corresponds to the (arbitrarily scaled) −2.5 horizontal flow isoline in Figure 8 (i.e., the value of the modeled isoline at the model coordinate corresponding to the velocity time series of Figure 10). Although observations do not exist with which to estimate wave-induced vertical displacement of the pycnocline, scaled model vertical velocity output suggests a vertical displacement amplitude of ∼17m for the 46 h period wave. Model output scaled in this way is used to estimate CTW-mediated exchange rates and CTW horizontal excursions in section 5.

Results so far may be summarized as follows: (1) CTWs are present within the KFT system, (2) CTWs are the dominant mode of harmonic current variability within the system, (3) CTW activity is principally a baroclinic Kelvin wave response, and (4) Significant seasonal variation in CTW properties is exhibited, with wavelength and phase speed doubling in summer as a result of stronger vertical stratification. This final statement is

based not on the sparse velocity data, but on the comprehensive stratification data presented in section 2. In section 5, we now go on to discuss fjordic exchange, and the implications that CTWs might have for fjord water properties.

5. Discussion

CTWs have been demonstrated to represent a major mode of flow variability within the fjord; we now ask "what is effect of CTWs on fjord exchange?" In a linear, inviscid world the answer might be "none," however, the introduction of mixing and finite amplitude effects raises the potential for significant CTW-induced exchange.

In the first part of the discussion, we identify the potential exchange processes in KFT, and attempt to place CTWs quantitatively in the context of overall exchange. To proceed systematically and consistently with standard terminology, an exchange or turnover time, T_{Ex} is defined as the time taken to renew $\sim$63% ($1 - 1/e$) of the total volume of the fjord, V, with water from outside the fjord, as mediated by process x [e.g., *Arneborg*, 2004; *Gillibrand*, 2001]. Since our focus is on exchange, an exchange rate for each process is defined as $Q_x = (1 - 1/e)V/T_{Ex}$, with units of m^{3}s^{-1} and is the metric used here for comparative purposes. With reference back to the introduction; Q_{bt} refers to barotropic pumping, Q_{est} to estuarine exchange, Q_{lat} to lateral circulation exchange, and Q_i to intermediate exchange. We note that with these definitions the total exchange is not necessarily additive, since Q_{lat} may encompass Q_{est} and elements of Q_i in a broad fjord.

In general, the exchange rate for inviscid oscillating flows, Q, is zero (although note that Stokes Drift is non-zero, see *Weber and Drivdal* [2012] and discussion below)—true for barotropic and baroclinic oscillatory flows alike. Geophysical flows in fjords are not inviscid, so it is convenient to define a mixing efficiency for barotropic and baroclinic (Q_{bt} and Q_i) pumping exchanges, with typical values of $\sim$68% (barotropic, [*Gillibrand*, 2001]) and $\sim$64% (baroclinic, [*Arneborg*, 2004]).

5.1. Barotropic Exchange
Following *Gillibrand* [2001], the barotropic tidal exchange rate is estimated as

$$Q_{bt} = \frac{eV_{KF}}{44928} \times \left(\frac{V_{KF} + RA_{KF}}{RA_{KF}(1 - \lambda_e)} \right)^{-1} \tag{5}$$

where $V_{KF} = 29.3$ km^3 is the fjord volume, $A_{KF} = 222$ km^2 the surface area, $R = 1$ m the tidal range (values from *Svendsen et al.* [2002]), $\lambda_e = 0.32$ accounts for the mixing efficiency, e$\sim$2.72 is the mathematical constant (Euler's number), and 44928 is the number of seconds per semidiurnal cycle. Evaluating equation (5) gives $Q_{bt} = 6.7 \times 10^3$ m^{3}s^{-1}, a value similar (to within a factor of 2) of that estimated by *Svendsen et al.* [2002] for Kongsfjorden.

5.2. Estuarine Exchange and Direct Wind-Driven Effects
The simplest way to estimate estuarine exchange, Q_e, is via the Knudsen relations. These combine conservation of salt and volume within the fjord, and observations of average salinity values in the upper and lower layer of a fjord to give an estuarine exchange estimate

$$Q_e = Q_f \frac{S_2}{(S_2 - S_1)} \tag{6}$$

where the freshwater discharge $Q_f = 43.4$ m^{3}s^{-1} [*Svendsen et al.*, 2002], and S_1 and S_2 are averaged upper and lower layer salinities, which take summer values of $S_1 = 32.1$ and $S_2 = 34.4$ derived from the historic database of Kongsfjorden CTD data. Evaluating equation (6) for typical summer values (when estuarine exchange will be maximal) gives $Q_e = 0.6 \times 10^3$ m^{3}s^{-1}. Interannual variations in Q_f are poorly known, however, seasonal variation has been estimated [*Svendsen et al.*, 2002], with $Q_{f\_max} = 60.3$, and therefore $Q_{e\_max} = 0.83 \times 10^3$ m^{3}s^{-1}. This maximal value is provided for reference, with the more appropriate mean value (albeit using a seasonal maximal Knudsen multiplier) retained for comparison with other averaged exchange terms. Related to the discussion of estuarine exchange in the upper layers of coastal systems, the influence of wind energy input into the surface layer needs to be considered, which may act to significantly retard (up-fjord wind) or enhance (down-fjord wind) estuarine exchange [e.g., *Moffat*, 2014]. Commonly

estimated is the Wedderburn number, first introduced [e.g., *Imberger and Hamblin*, 1982] to express the force balance between wind stress and pycnocline tilt in lakes, and extended later to express the balance between density driven (estuarine, in our context) and wind-induced interfacial mixing [*Monismith*, 1986]. The expression has curiously been inverted more recently [*Geyer*, 1997; *Thorpe*, 2005] and we use that form

$$W = \frac{\tau_x L_{KF}}{\Delta \rho g H_1^2} \tag{7}$$

where τ_x is the along-ford wind stress, $L_{KF} = 25$ km is the fjord length, $\Delta \rho = 1.6$ kgm^{-3} is a typical summer time upper layer density difference along the fjord axis (derived from the CTD database for August and September), $H_1 = 40$ m is a typical summer vertical scale for the freshened surface layer [*Cottier et al.*, 2005]. Evaluating equation (7) using maximal historic wind stress values of $\tau_x \sim 0.25$ Nm^{-2} [*Svendsen et al.*, 2002] gives $W \sim 0.26$, indicating that in summer the surface density gradient driven baroclinic (estuarine) exchange flows will dominate over wind driven effects. In winter, this situation is likely to change as peak wind stress observation in February and March [*Svendsen et al.*, 2002] coincide with reduced, or absent density forcing.

5.3. Hydraulic Control and Internal Tides

In macrotidal fjordic systems with shallow sills or systems with sills of comparable depth to the estuarine exchange flows, internal hydraulic effects may exert control on two layer exchange flows [*Farmer and Armi*, 1986]. The KFT system is neither macrotidal, nor has a significant sill. Densimetric Froude numbers can be defined for both the estuarine and tidal fjord-mouth flows as

$$F_p = \frac{U_p}{\sqrt{g'd}} \tag{8}$$

where U_p is the magnitude of flow (p is the process, estuarine or tidal) at the sill, d is the sill depth, and g' is reduced gravity for two layer flow at the sill. Expressed this way the densimetric Froude number nondimensionalises the flow speed in question (estuarine or tidal) with respect to the speed of the fastest linear internal wave mode; as F approaches one, hydraulic control effects on baroclinic exchange are likely. Using a fjord cross-sectional area at the sill of $B_m d$, ($B_m = 10$ km, and $d = 200$ m), and a fresh water discharge $Q_f = 43.4$ m^{3}s^{-1} and typical summer stratification ($\sqrt{g'd} = 0.5$ ms^{-1}), gives $F_{est} = 3 \times 10^{-5}$. For tidal flows, using the fjord geometry and tidal range already stated ($A_{KF} = 222$ km^2, $R = 1$ m), gives $F_{tide} = 0.02$. Both densimetric Froude numbers are much less than one, demonstrating that hydraulic effects are not important in this system.

In addition to this scaling argument, direct evidence that internal tides are very weak in this system is found using the mooring data of *Cottier et al.* [2005], which measured full depth current profiles every 20 min near the mouth of the fjord system during summer 2002 (location S3 marked on Figure 2). Depth-averaged baroclinic energy spectral levels computed at S3 are more than one order of magnitude below the open ocean levels of the canonical Garret and Munk spectrum [*Desaubies*, 1976]. This is in stark contrast to typical tidally energetic shelf systems [e.g., *Inall et al.*, 2000, Figure 5].

5.4. Lateral Exchange

One element of lateral exchange is a manifestation of the influence of rotation on baroclinic exchange flows in a broad fjord (e.g., estuarine exchange), and therefore not an additional exchange mechanism per se. Examples of this have been shown in Kongsfjorden [*Svendsen et al.*, 2002], in the Clyde Sea system of western Scotland [*Janzen et al.*, 2005], and in Porsangerfjord in northern Norway [*Cushman-Roisin et al.*, 1994]. An element of lateral exchange not yet considered is topographic steering of steady geostrophic flows around the interior perimeter of a wide fjord. The eastward transport of Atlantic-origin water on the southern slope of the Isfjorden Trough has been estimated, using a barotropic model, to be O(0.02) Sv, or 2×10^4 m^{3}s^{-1} [*Nilsen et al.*, 2015]. A comparable figure for the KFT is not available, though it might be similar given the similar geometries of the troughs. However, how such a flow might communicate further into the interior perimeter of the fjord if the flow is not topographically guided into the fjord (i.e., week front/geostrophic control) is completely unknown.

Table 4. Fjordic Nondimensional Parameters W (Wedderburn Number), F (Estuarine and Tidal Densimetric Froude Numbers), and Exchange Estimates for Kongsfjord[a]

Parameters ([Q] m^{3}s^{-1})	W	F_{est}	F_{tide}	Q_{bt}	Q_{est}	Q_{lat}	Q_i	$Q_i^{CTW\_ave}$
	0.26 (peak)	3×10^{-5}	0.02	2.5×10^3	0.62×10^3	?	2.4×10^4	0.82×10^4

[a]See text for definitions. Exchange rates have units of m^{3}s^{-1}. Q_{bt} refers to barotropic pumping, Q_{est} to estuarine exchange, Q_{lat} to lateral circulation exchange, and Q_i to intermediate exchange estimated using equation (9). Total exchange is not necessarily additive, since Q_{lat} may encompass Q_{est} and elements of Q_i in a broad fjord.

5.5. Intermediary Exchange

The term intermediary exchange is a "catch-all" descriptor for unsteady (on some undefined time scale) density-driven exchange flow beneath the estuarine exchange. Any process giving rise to a deep pressure gradient between fjord and adjacent coast will have the potential to contribute to an intermediary exchange. An expression for the magnitude of intermediary exchange driven by variations in coastal density can be written [*Aure et al.*, 1996] as

$$Q_i = \beta V_{KF}^{-1} \left(B_m d A_{KF} \frac{g\Delta M}{\rho} \right)^{1/2} \tag{9}$$

where V_{KF}, B_m, d, A_{KF} are fjord geometries (volume above sill depth, width, entrance depth, surface area; as previously defined), $\beta = 17 \times 10^{-4}$ is an empirical constant, ρ is the density of shelf water, and ΔM is the standard deviation of the weight M (kgm^{-2}) of a shelf water column from the mean sea surface down to sill depth. Using all summer density profiles in the database from the entrance to KF (a total of 85 profiles), ΔM was evaluated as the vertical integral of the standard deviation of $\rho(z)$ from the surface to 250 m (taken to be the nominal sill depth), giving $Q_i = 2.35 \times 10^4$ m^{3}s^{-1}. This value is comparable to estimates calculated in the same way for two larger SE Greenland fjords [*Sutherland et al.*, 2014]. The disadvantage of equation (9) is that it contains no information on the time scale(s) of the process(es) contributing to Q_i and so a mechanistic understanding of what is driving this exchange is absent. In the only long-term analysis of intermediary fjordic exchange, we are aware of (in Gullmarfjord) [*Arneborg*, 2004], it is notable that Q_i is dominated by fluctuations of order ± 4000 m^{3}s^{-1} with periods of 1–5 days. Scaled by fjord mouth cross-sectional area, these are similar values to those found here and in SE Greenland using equation (9), but more interesting is the dominance of the 1–5 day period fluctuations. It should be noted however that there is no discussion by *Arneborg* [2004] on how external pycnocline displacements might be communicated into the fjord, nor whether the fluctuations are a wave phenomenon.

We do not have sufficient observational data here to directly evaluate CTW-driven intermediary exchange, Q_i^{CTW}, but we can use the observationally scaled model output to make such an estimate.

$$Q_i^{CTW} = 0.64 \frac{4}{\pi} \int \int_{z=-h}^{z=-h_i} U(x,z) dx dz \tag{10}$$

where $U(x,z)$ is the scaled wave velocity amplitude, the integral is across the isobaths and over the lower layer (defined by the zero crossing of $U(z)$), $2/\pi$ accounts for an integer half wave-period time average and the additional factor of 2 accounts for the upper layer (equal in magnitude to the lower layer), and the 0.64 accounts for the efficiency with which water advected in or out of the fjord is modified by mixing [*Arneborg*, 2004]. Evaluating equation (10) for the scaled model CTW of Figure 8 gives $Q_i^{CTW} = 6.8 \times 10^4$ m^{3}s^{-1}. To be clear, this estimate of Q_i^{CTW} is only meaningful during periods of time when the waves are active, but it serves to illustrate the exchange capacity of CTWs. Further consideration of the wavelet analysis reveals that CTWs are present during 15% of the summer record (Figure 6a) and during 9% of the winter record (Figure 6b). These estimates are the percentage of the time that the scale-averaged variance (averaged between 40 and 60 h) exceeds the 95% confidence level. They allow a year-long time-averaged exchange effect of the CTWs to be estimated as 12% of Q_i^{CTW}: i.e., $Q_i^{CTW\_ave} \sim 0.82 \times 10^4$ m^{3}s^{-1}, or around one third of Q_i evaluated using equation (9), strongly suggesting that CTWs are a significant contributor to the total intermediary exchange; a key result of this study.

The various exchange estimates calculated above are drawn together in Table 4, and the foregoing discussions may be summarized as follows: surface layer flows are largely dominated by estuarine circulation,
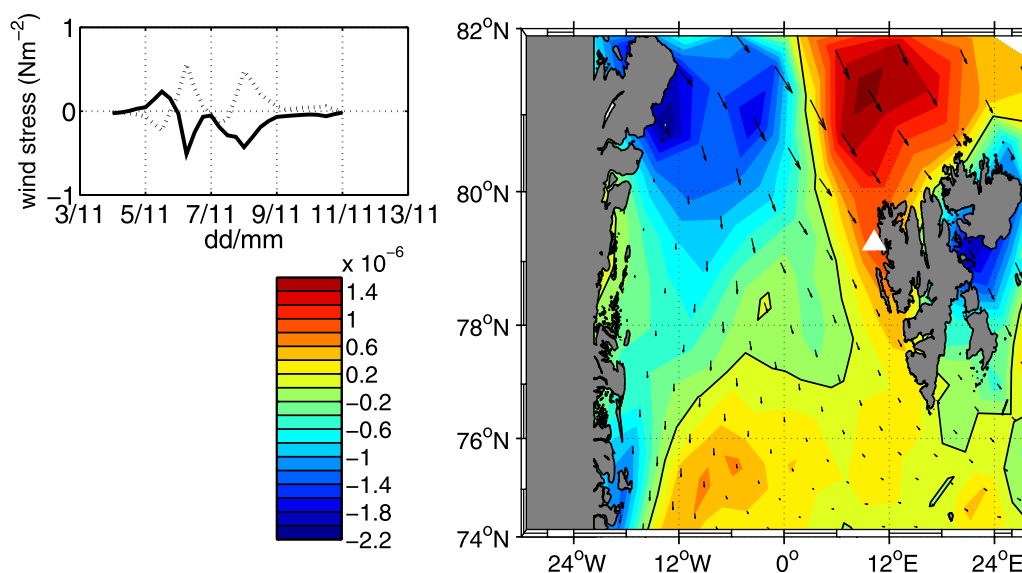
Figure 13. Main colour plot: ERA Interim analysis wind stress curl (Nm^{-3}) over the region, averaged over the period 4–11 November 2004. Inset: wind stress (Nm^{-2}) at the mouth of KFT (line plot), location illustrated with a white triangle on main plot. Northerly component (solid line) and easterly component (dashed line), for the period 4–11 November 2004.

with wind-driven effects secondary (peak $W \sim 0.26$) in summer. Internal hydraulics do not control exchange (tidal and estuarine densimetric Froude numbers $\ll 1$), and internal tides and baroclinic kinetic energy are generally very weak. Of the estimated exchange terms, estuarine exchange is weakest ($Q_{est}=0.62\times10^3$ m^{3}s^{-1}), followed by barotropic tidal pumping ($Q_{bt}=2.5\times10^3$ m^{3}s^{-1}), with intermediary exchange dominating ($Q_i=2.4\times10^4$ m^{3}s^{-1}). Wavelet analysis (Figures 6a and 6b) indicates that oscillating flows displayed greatest activity in the 1–5 day period band. CTW activity has been identified as the likely source of variability in the 40–60 h period band, and in that band intermediary exchange is estimated as $Q_i^{CTW\_ave}=0.82\times10^4$ m^{3}s^{-1}, exceeding both barotropic and estuarine exchange estimates.

Having established the position of CTWs in the hierarchy of fjord exchange mechanisms, we continue now in this discussion to examine a potential generation mechanism for CTWs, and their propagation as the transient response to a pycnocline perturbation some distance away.

5.6. Forcing Mechanism
From 5 to 8 November 2004, a vigorous low-pressure system passed over the entrance to KFT from a (south) westerly direction (Figure 13). Two peaks in wind stress occurred over a 48 h period, reaching values in excess of 0.5 Nm^{-2} in each peak, with the winds at the fixed location of KFT rotating anticyclonically between the peaks consistent with low pressure centerd to the north of KFT and tracking from west to east. The first peak in south-easterly wind stress (wind from the southeast) occurred at 12:00UTC on 5 November inducing a convergent surface Ekman flow toward the coast with an downwelling response time of order 1/f (12.2 h at 79°N), leading to an assumed depression of the pycnocline under the storm track at the shelf break. This was followed by the opposite wind direction, and assumed opposite pycnocline response (i.e., upwelling), in two peaks centerd some 40 h later. Between 8 and 11 November, energetic CTW activity was recorded in the fjord (Figure 11), with an estimated phase speed of $C_p \sim 0.25$ ms^{-1} at the moorings. The first peak of increased upper layer inflow occurred at 04:00UTC on 8 November, consistent with a falling interface. The phase speed in deep water seaward of the moorings was likely greater, given that the waves are long (nondispersive). A 64 h lag between the first wind stress peak and the arrival of strong CTW-induced velocities at mooring S2 is consistent with a wave (of initial downward perturbation) propagating at a speed of approximately 0.28 ms^{-1} from the shelf break to the mooring (a distance of $\sim$65 km); suggestive of a CTW phase speed a little in excess of the averaged estimate from the relatively shallow mooring of $C_p = 0.25$ ms^{-1}, consistent with long waves slowing due to topographic shoaling.

Weather systems such as this are a relatively common winter feature in the Fram Strait region. They are more frequent and intense during autumn and winter, although by no means confined to these seasons [*Rogers et al.*, 2005].

A second point regarding the generation mechanisms for CTWs echoes the work of *Johnson and Marshall* [2002] who discuss CTWs as the fastest agent of remotely communicating an adjustment to a high-latitude pycnocline perturbation. In their case, they discussed the communication, via baroclinic Kelvin wave propagation southward along an ocean boundary, of a high-latitude pycnocline elevation perturbation forced by increased deep convection. The CTW wind-forcing mechanism described above, that of a localized wind forced pycnocline elevation lasting several tens of hours, will have a transient response (the propagating CTWs) and a modified geostrophically balanced residual response. The appearance of CTWs within a fjord may well therefore precede an adjustment to the preexisting baroclinic geostrophic state of the system, whether it be inhibiting fjord shelf exchange or further enhancing it.

From our observations, CTW wave periods are similar throughout the 1 year of observation, corresponding to a forced CTW response (i.e., nonresonant) at a frequency responding to the inverse passage period of weather systems. Stronger summer stratification gives rise to longer and faster CTWs at the same frequency compared to winter (see Figure 7, dispersion diagram). As hinted at above, stronger forcing coupled with weaker stratification may combine to increase the transient effect of CTWs on fjord/shelf exchange in winter compared with summer. In relation to seasonality, we note that the lowest horizontal mode baroclinic seiche period (one quarter wavelength) in Kongsfjord varies from between $T_{seiche} \sim 200$ h in the winter, and $T_{seiche} \sim 100$ h in summer, taking a fjord length of $L = 40$ km and $c = 0.25$ (0.5) ms^{-1} for summer (winter). It seems unlikely, therefore, that CTWs forced by the passage of a low-pressure system will resonate in the fjord during winter. Resonance may well be possible in summer with increase stratification combined with the slower passage of a weather system, or in other systems of differing geometry.

5.7. Advective Excursion
Using the observationally scaled model fields gives maximum wave-induced particle velocities of ~ 0.30 ms^{-1} above the shallow region of the slope. Here, then, on the upper slopes the corresponding advective excursion over one half of a wave period ($L_{ex} = TU/\pi$) is 16 km (with $T = 46$ h and $U = 0.3$ ms^{-1}), illustrating the considerable distance particles in the upper water column could be oscillated during the passage of CTWs. Currents of this magnitude (0.2–0.3 ms^{-1}) are also likely to resuspend material from the bed on the upper slopes (down to around 100 m, where the horizontal velocities decrease more rapidly), and generate a turbulent bottom boundary. Boundary mixing will also ensure that CTWs do not simply move the same water into, and then back out of the fjord. Rather (by analogy with tidal flows in macro-tidal fjords) an enhancement to the exchange between fjord and shelf waters will result, and it is these irreversible processes that contribute to the mixing efficiency (64%) [*Arneborg*, 2004] used earlier to quantify $Q_i^{CTW\_ave}$. We do note, however, that the estimates of both barotropic and baroclinic (intermediary) exchange depend on the values used for mixing efficiencies, derived from a relatively small number of fjord studies.

5.8. Stokes Drift
The final wave effect to be discussed is that of the wave-induced Stokes drift. To the best of the authors' knowledge, Stokes drift induced by CTWs propagating along a sloping boundary has not been formally investigated in the literature. The case of Stokes drift within freely propagating internal waves was first described by *Thorpe* [1968], and the trapped internal Kelvin wave case by *Wunsch* [1973]. More recently analytic and numerical Stokes drift and mean Eulerian drift calculations have been presented for internal Kelvin waves under an ice-covered boundary [*Stoylen and Weber*, 2010]. Noting that the CTWs observed here are predominantly Kelvin-like (with a small vorticity component), equation (20) of *Stoylen and Weber* [2010] can be evaluated to give an estimate of the Stokes drift, $\overline{U_s}$, in a region close to the KFT sloping boundary.

$$\overline{U_s} = \frac{C_p A^2}{2 H_1 H_e} e^{-2(y/a)} \tag{11}$$

where, H_e is the effective depth for a two later system, a is the Rossby deformation radius and other variables are as previously defined. Substituting appropriate values of $H_e = 75$ m (CTW zero crossing at ~ 150 m, so $H_1 = H_2 = 150$ m), phase speed $C_p = 0.25$–0.5 ms^{-1} and a interfacial wave amplitude of $A = 17$ m, gives a Stokes drift of O($+0.007$ to $+0.014$ ms^{-1}) in the upper layer in the vicinity of the coastal boundary ($y = 0$);

equivalent to a mean advection in the upper layer in the direction of wave propagation of approximately 1.6–3.2 km over one wave period (46 h). Though this is a relatively small distance, if CTWs are maintained for many wave periods, then a mean advection over tens kilometres may result.

6. Conclusions

In this article, we have shown CTWs to be a dominant mode of flow variability and a significant contributor to water volume exchange in the KFT system, exceeding wind, estuarine, and tidal (barotropic and baroclinic) effects. The phenomena, and the direct consequences discussed are unlikely to be restricted to KFT. There are good reasons to anticipate that CTWs will be a dominant source of variability all around the Svalbard and Greenland ocean margins and adjacent fjords; areas where similar conditions of weak external tides, deep fjords, and vigorous atmospheric pressure systems prevail.

References

Allen, J. S. (1975), Coastal trapped waves in a stratified ocean, *J. Phys. Oceanogr.*, 5, 300–325.

Arneborg, L. (2004), Turnover times for the water above sill level in Gullmar Fjord, *Cont. Shelf Res.*, 24(4–5), 443–460.

Aure, J., J. Molvaer, and A. Stigebrandt (1996), Observations of inshore water exchange forced by a fluctuating offshore density field, *Mar. Pollut. Bull.*, 33(1), 112–119, doi:10.1016/S0025-326X(97)00005-2.

Battisti, D. S., and B. M. Hickey (1984), Application of remote wind-forced coastal trapped wave theory to the oregon and washington coasts, *J. Phys. Oceanogr.*, 14, 887–903.

Boyd, T. J., and A. E. D'Asaro (1994), Cooling of the West Spitzbergen current: Wintertime observations west of Svalbard, *J. Geophys. Res.*, 11, 22,597–522,618.

Brink, K. H. (1982), A comparison of long coastal-trapped wave theory with observations off Peru, *J. Phys. Oceanogr.*, 12, 897–913.

Cottier, F. R., V. Tverberg, M. E. Inall, H. Svensen, F. Nilsen, and C. R. Griffiths (2005), Water mass modification in an Arctic fjord through cross-shelf exchange: The seasonal hydrography of Kongsfjorden, Svalbard, *J. Geophys. Res.*, 110, C12005, doi:10.1029/2004JC002757.

Cottier, F. R., F. Nilsen, M. E. Inall, S. Gerland, V. Tverberg, and H. Svendsen (2007), Wintertime warming of an Arctic shelf in response to large-scale atmospheric circulation, *Geophys. Res. Lett.*, 34, L10607, doi:10.1029/2007GL029948.

Cottier, F. R., F. Nilsen, R. Skogseth, V. Tverberg, J. Skardhamar, and H. Svendsen (2010), Arctic fjords: A review of the oceanographic environment and dominant physical processes, *Geol. Soc. Spec. Publ.*, 344, 51–60.

Cushman-Roisin, B., L. Asplin, and H. Svendsen (1994), Upwelling in broad fjords, *Cont. Shelf Res.*, 14(55), 1701–1721.

Dale, A. C., J. Huthnance, and T. J. Sherwin (2001), Coastal-trapped waves and tides at near-inertial frequencies., *J. Phys. Oceanogr.*, 31(10), 2958–2970.

Dee, D. P., et al. (2011), The ERA-Interim reanalysis: Configuration and performance of the data assimilation system, *Q J R. Meteorol. Soc*, 137(656), 553–597, doi:10.1002/qj.828.

Desaubies, Y. J. F. (1976), Analytical representation of internal wave spectra, *J. Phys. Oceanogr.*, 6(6), 976–981, doi:10.1175/1520-0485(1976)006$<$0976:AROIWS$>$2.0.CO;2.

Edwards, A., and D. Edelsten (1977), Deep water renewal of Loch Etive: A three basin Scottish fjord, *Estuarine Coastal Mar. Sci.*, 5(5), 575–595.

Farmer, D. M., and L. Armi (1986), Maximal two-layer exchange over a sill and through the combination of a sill and contraction with barotropic flow, *J. Fluid Mech.*, 164, 53–76.

Geyer, W. R. (1997), Influence of wind on dynamics and flushing of shallow estuaries, *Estuarine Coastal Shelf Sci.*, 44(6), 713–722, doi:10.1006/ecss.1996.0140.

Gillibrand, P. A. (2001), Calculating exchange times in a Scottish fjord using a two- dimensional, laterally-integrated numerical model, *Estuarine Coastal Shelf Sci.*, 53(4), 437–449.

Gjevik, B., and T. Straume (1989), Model simulations of the M2 and K1 tide in the Nordic seas and Arctic Ocean, *Tellus Ser. A*, 41, 73–96.

Gonella, J. (1972), Rotary-component method for analyzing meteorological and oceanographic vector time series, *Deep Sea Res. Oceanogr. Abstr.*, 19(12), 833–846, doi:10.1016/0011-7471(72)90002-2.

Huthnance, J. M. (1978), On coastal trapped waves: Analysis and numerical calculation by inverse interation, *J. Phys. Oceanogr.*, 8, 74–92.

Imberger, J., and P. F. Hamblin (1982), Dynamics of lakes, reservoirs, and cooling ponds, *Annu. Rev. Fluid Mech.*, 14(1), 153–187, doi:10.1146/annurev.fl.14.010182.001101.

Inall, M. E., and P. A. Gillibrand (2010), The physics of mid-latitude fjords: A review *Geol. Soc. Spec. Publ.*, 344, 17–33, doi:10.1144/SP344.3.

Inall, M. E., T. P. Rippeth, and T. J. Sherwin (2000), Impact of nonlinear waves on the dissipation of internal tidal energy at a shelf break, *J. Geophys. Res.*, 105, 8687–8705.

Inall, M. E., T. Murray, F. Cottier, K. Scharrer, T. J. Boyd, K. J. Heywood, and S. L. Bevan (2014), Oceanic heat delivery via Kangerlugssuaq fjord to the south-east Greenland ice sheet, *J. Geophys. Res. Oceans*, 119, 631–645, doi:10.1002/2013JC009295.

Jakobsson, M., et al. (2012), the international bathymetric chart of the arctic ocean (IBCAO) Version 3.0, *Geophys. Res. Lett.*, 39, L12609, doi:10.1029/2012GL052219.

Janzen, C. D., J. H. Simpson, M. E. Inall, and F. Cottier (2005), Across-sill circulation near a tidal mixing front in a broad fjord, *Cont. Shelf Res.*, 25(15), 1805–1824, doi:10.1016/j.csr.2005.06.004.

Johnson, H. L., and D. P. Marshall (2002), A theory for the surface atlantic response to thermohaline variability, *J. Phys. Oceanogr.*, 32, 1121–1132.

Klinck, J. M., J. J. O'Brien, and H. Svendsen (1981), A simple model of fjord and coastal circulation interaction, *J. Phys. Oceanogr.*, 11, 1612–1626.

Livingstone, D., and T. C. Royer (1980), Observed surface winds at middleton island, gulf of alaska and their influence on the ocean circulation, *J. Phys. Oceanogr.*, 10(5), 753–764.

Moffat, C. (2014), Wind-driven modulation of warm water supply to a proglacial fjord, Jorge Montt Glacier, Patagonia, *Geophys. Res. Lett.*, 41, 3943–3950, doi:10.1002/2014GL060071.

Monismith, S. (1986), An experimental study of the upwelling response of stratified reservoirs to surface shear stress, *J. Fluid Mech.*, *117*, 407–493.

Mysak, L. A. (1980), Topographically trapped waves, *Annu. Rev. Fluid Mech.*, *12*, 45–76.

Nilsen, F., B. Gjevik, and U. Schauer (2006), Cooling of the West Spitsbergen Current: Isopycnal diffusion by topographic vorticity waves, *J. Geophys. Res.*, *111*, C08012, doi:10.1029/2005JC002991.

Nilsen, F., F. Cottier, R. Skogseth, and S. Mattsson (2008), Fjord-shelf exchanges controlled by ice and brine production: The interannual variation of Atlantic Water in Isfjorden, Svalbard, *Cont. Shelf Res.*, *28*(14), 1838–1853, doi:10.1016/j.csr.2008.04.015.

Nilsen, F., R. Skogseth, J. Vaardal-Lunde, and M. E. Inall (2015), A simple shelf circulation model: Intrusion of atlanticwater on the west spitsbergen shelf, *J. Phys. Oceanogr.*, in press.

Padman, L., and S. Erofeeva (2004), A barotropic inverse tidal model for the Arctic Ocean, *Geophys. Res. Lett.*, *31*, L02303, doi:10.1029/2003GL019003.

Proehl, J. A., and M. Rattray (1984), Low-frequency response of wide deep estuaries to non-local atmospheric forcing, *J. Phys. Oceanogr.*, *14*, 904–921.

Rippeth, T. P., and J. H. Simpson (1996), The frequency and duration of episodes of complete vertical mixing in the Clyde Sea, *Cont. Shelf Res.*, *16*(7), 933–947.

Rogers, J. C., L. Yang, and L. Li (2005), The role of Fram Strait winter cyclones on sea ice flux and on Spitsbergen air temperatures, *Geophys. Res. Lett.*, *32*, L06709, doi:10.1029/2004GL022 262.

Roussenov, V. M., R. G. Williams, C. W. Hughes, and R. J. Bingham (2008), Boundary wave communication of bottom pressure and overturning changes for the North Atlantic, *J. Geophys. Res.*, *113*, C08042, doi:10.1029/2007JC004501.

Stigebrandt, A. (1990), On the response of the horizontal mean vertical density distribution in a fjord to low-frequency density fluctuations in the coastal water, *Tellus Ser. A*, *42*, 605–614.

Stigebrandt, A. (2001), Fiord circulation, in *Encyclopedia of Ocean Sciences*, edited by J. Steele, K. Turekian, and S. A. Thorpe, pp. 897–902, Academic, Oxford.

Stigebrandt, A. (2012), Hydrodynamics and circulation of Fjords, in *Encyclopedia of Lakes and Reservoirs*, edited by L. Bengtsson, R. Herschy, and R. Fairbridge, pp. 327–344, Springer, Netherlands, doi:10.1007/978-1-4020-4410-6_247.

Stoylen, E., and J. E. H. Weber (2010), Mass transport induced by internal Kelvin waves beneath shore-fast ice, *J. Geophys. Res.*, *115*, C03022, doi:10.1029/2009JC005298.

Sutherland, D. A., and F. Straneo (2012), Estimating ocean heat transports and submarine melt rates in Sermilik Fjord, Greenland, using lowered acoustic Doppler current profiler (LADCP) velocity profiles, *Ann. Glaciol.*, *53*(60), 50–58, doi:10.3189/2012AoG60A050.

Sutherland, D. A., F. Straneo, and R. S. Pickart (2014), Characteristics and dynamics of two major Greenland glacial fjords, *J. Geophys. Res. Oceans*, *119*, 3767–3791, doi:10.1002/2013JC009786.

Svendsen, H., et al. (2002), The physical environment of Kongsfjorden-Krossfjorden, an Arctic fjord system in Svalbard, *Polar Res.*, *21*(1), 133–166.

Teigen, S. H., F. Nilsen, and B. Gjevik (2010), Barotropic instability in the West Spitsbergen Current, *J. Geophys. Res.*, *115*, C07016, doi:10.1029/2009JC005996.

Thorpe, S. A. (1968), On the shape of progressive internal waves, *Philos. Trans. R. Soc. A*, *263*, 563–614.

Thorpe, S. A. (2005), *The Turbulent Ocean*, 439 pp., Cambridge Univ. Press, London, U. K.

Weber, J. E. H., and M. Drivdal (2012), Radiation stress and mean drift in continental shelf waves, *Cont. Shelf Res.*, *35*, 108–116, doi:10.1016/j.csr.2012.01.001.

Wunsch, C. (1973), On the mean drift in large lakes, *Limnol. Oceanogr.*, *18*(5), 793–795.